Arabian Journal for Science and Engineering (2018) 43:6315–6324
https://doi.org/10.1007/s13369-017-3032-y

RESEARCH ARTICLE - PETROLEUM ENGINEERING

Experimental Measurements of Shale Fracture Conductivity Under Cyclic Loading

Honglian Li[1,2] · Jiren Tang[1,2] · Yiyu Lu[1,2] · Lei Zhou[1,2] · Shuaibin Han[1,2] · Rui Dai[3]

Received: 25 July 2017 / Accepted: 5 December 2017 / Published online: 21 December 2017

Abstract
Existing research on shale fracture conductivity is rather sparse and has not taken the effect of loading history into consideration. A splitting device was used to split the shale specimens along bedding, and a 3D scanner was used to characterize the fracture surface. Using a constant 0.3 MPa gas pressure, three shale specimens split by single fractures of different roughness were tested for gas flow during four loading–unloading cycles of 0–10 MPa. Test results show that fracture conductivity exhibited hysteresis similar to that observed in rock mechanics experiments. In addition, it is clear that fracture conductivity is smaller for fractures with rougher surfaces. Building on the cubic law and soil mechanics consolidation theory, a hydraulic aperture model for cyclic loading was developed that helps explain the influence of plastic deformation during loading and unloading on fracture conductivity. This model exhibited trends get the agreement with the data for the range of confining stresses used in the experiments.

Keywords Shale fracture conductivity · Cyclic loading · Surface roughness · Hydraulic aperture model

1 Introduction

A shale reservoir has low permeability. Generally, it can only produce economic production of gas from shales after being fractured to generate an artificial fracture network [1]. The limited proppant-carrying ability of fracturing fluid prevents proppants from moving into the natural fracture system. The primary fractures have a amount of proppants, and natural fractures are proppant-less [2]. If the proppants are not placed in the proper areas of the artificial fracture network, the flow conductivity of nature fracture will directly determine the effectiveness of the artificial fracture network in shale reservoir and the shale gas production [3].

Fracture conductivity has been studied since the early 1970s. On the basis of the Navier–Stokes equation, Lomize [4] deduced the cubic law and introduced the concept of fracture hydraulic aperture. Kranz [5] found that the fracture conductivity of rock is affected by the effective stress and the roughness of fracture surfaces. Through experimental research on fractures in granite, marble, and basalt, Gale [6] discovered the negative exponential relationship between fracture conductivity and effective stress. By introducing the ratio between fracture contact area and fracture area, Tsang [7] revised the cubic law. Thompson [8] studied the relationship between fracture aperture and effective flow width using a fractal model for fractures. Barton [9–11] researched the influence of effective stress on the hydraulic aperture of fractures and proposed a relationship between hydraulic aperture and mechanical aperture. Zimmerman [12,13] investigated the effect of fracture surface roughness and fracture contact area on conductivity and found that the fracture conductivity is not only related to the fracture contact area but also influenced by the shape of the asperities on the fracture surface. However, existing research on shale fracture conductivity is rather sparse and has not taken the effect of loading history into consideration [14,15].

Real shale reservoirs are not only affected by gravitational stresses imposed by the overlying strata and horizontal crustal and tectonic stresses; the reservoirs are also influenced by secondary stress brought on by underground operations

✉ Jiren Tang
tangjiren@cqu.edu.cn

1 State Key Laboratory of Coal Mine Disaster Dynamics and Control, Chongqing University, Chongqing 400044, China

2 National and Local Joint Engineering Laboratory of Gas Drainage in Complex Coal Seam, Chongqing University, Chongqing 400044, China

3 East Sichuan Drilling Company of CNPC Chuanqing, Chongqing 400021, China

like staged fracturing in nearby shale well section. In staged fracturing of shale gas well, when one section of the reservoir is being fractured, horizontal crustal stress in that sections will increase and produce lateral stresses in neighboring sections. This will cause existing fractures in the neighboring well sections to close due to the increased effective stress from the adjacent section. As the fracture fluid flows back during staged fracturing [16], the crustal stress in the section being fractured will decrease; hence, the force exerted on the neighboring well sections will also decrease. Fractures in those sections may open and for a fracture network, this is unloading caused by decreased effective stress. During gas well production, because of this cyclic loading, the porous media and fluid are undergoing alternating periods of swelling and shrinking, stress–strain conditions are fluctuating, and the effective stress on fractures is alternating between loading and unloading. Therefore, reservoir fractures may be subjected to complicated loading cycles [17].

This paper describes the results from laboratory experiments designed to explore the influence of effective stress, loading history, and fracture surface roughness on shale fracture conductivity. A Brazilian splitting device was used to split the Sichuan-Longmaxi shale specimens with a fracture along the bedding plane, a 3D laser scanner was used to analyze the fracture surface roughness, and a triaxial compression testing system was used to determine fracture conductivity under cyclic loading. The hysteresis of the shale fracture hydraulic aperture during loading and unloading is discussed, and based on the experimental results, a model for fracture hydraulic aperture that takes the loading history into consideration is put forward.

2 Laboratory Equipment and Experimental Procedures

2.1 Specimens

The shale used in the experiments was collected from an outcrop of the Longmaxi group in the east part of the Sichuan Basin, China. According to the X-ray analysis [18], the shale is composed of 52.1% quartz, 23.6% calcite, 8.8% clay, 8.4% dolomite, 3.6% pyrite, 2.5% plagioclase, and 1% unidentified phases. The rock is relatively brittle. Specimens for testing were prepared by coring a shale specimen parallel to bedding and then cutting the core to ϕ50 mm $\times$ 100 mm standard cylindrical samples (Fig. 1). Figure 2 shows the custom-made Brazilian device. The core is placed on the pedestal of this device and then rotated until the bedding planes are parallel to the loading direction. By exerting an external load, the shale specimen can be split by a single fracture along a bedding plane. After splitting, the length and width of the fracture surface are measured and its nominal surface area calculated.

2.2 Experimental Equipment

To investigate the influence of fracture surface roughness on fracture conductivity from a microscopic perspective, the fracture surfaces of three specimens were scanned. The scanner, a high-precision 3D laser scanner, produces two mega-pixel images, which has a scanning dot spacing of 0.1 mm and a scanning precision of 0.02 mm. Flow experiments were conducted at the State Key Laboratory of Coal Mine Disaster Dynamics and Control, Chongqing University, China. The experiments were performed on a triaxial servo test system (Fig. 3), experimental equipment for investigating the physical and mechanical properties of rock in com-

Fig. 1 Photograph of shale specimens before testing

plicated environments. The equipment, a servo-controlled compression testing machine, can reach a maximum axial load of 2000 KN, a maximum confining pressure of 30 MPa, and a maximum gas pressure of 2 MPa with a test precision of ± 1% and a control accuracy of ± 0.5%. The test system can perform uniaxial, triaxial, cyclic loading, and flow experiments. During testing, the axial load is provided by a hydraulic ram, an electric oil pump furnishes the confining load, and the gas pressure is provided from a gas cylinder and a reducing valve. During experiments, the readings for axial load and confining pressure are automatically collected by the computer system and gas flow is measured by a digital electronic flow meter.

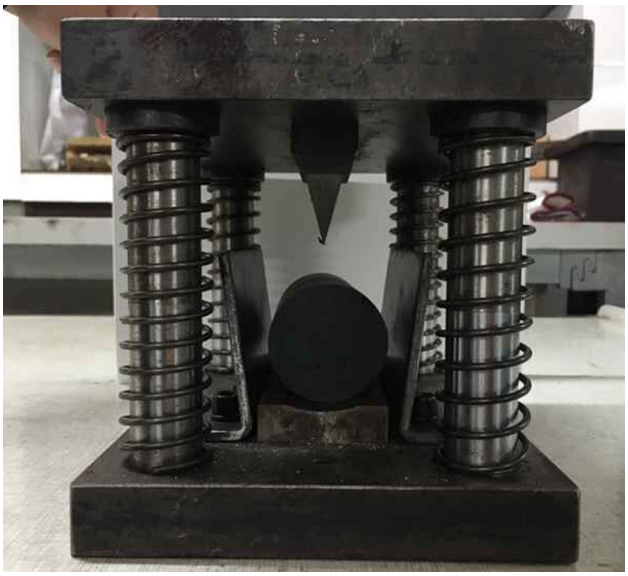

Fig. 2 Photograph of the custom-made shale splitting device with a specimen ready for splitting

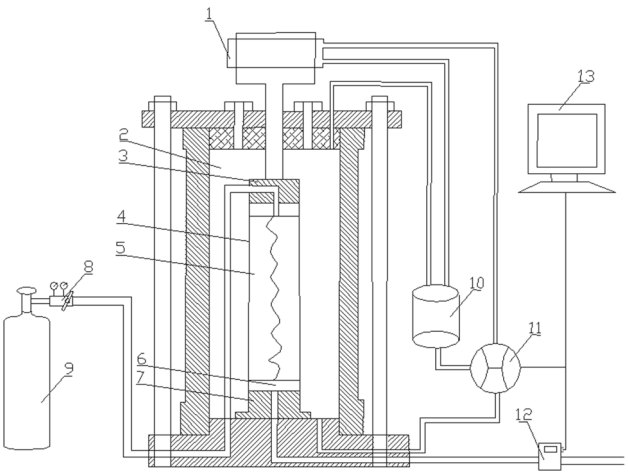

Fig. 3 Schematic diagram of the triaxial servo test system. *1* Axial loading; *2* oil chamber; *3* top pedestal; *4* latex membrane; *5* sample; *6* porous platen; *7* base pedestal; *8* pressure reducing valve; *9* compressed gas tank (methane); *10* oil reservoir; *11* hydraulic pressure pump; *12* gas flow meter; *13* Computer

2.3 Experimental Procedure

Silicon rubber is applied to fill any fractures on the specimen evenly. After the silicon rubber has completely dried, the irregular silicon rubber on the outside wall of specimen is moderately pared. Then, the specimen is placed on the triaxial cell's supporting seat and covered with a rubber membrane. The compression piston rod is placed on the rock specimen, and a hair dryer is used to tighten the rubber membrane to ensure that the specimen completely sealed. Two clamps with O-rings were placed on the top and the bottom pedestals over the membrane to avoid leakage and to fix the sample in the cell. After that, the cell was closed and filled with silicon oil. A vacuum pump is connected to extract the air from the specimen, and then, the preset confining pressure and axial pressure are applied.

For these experiments, there was no axial pressure head displacement and the specimen's axial deformation was constrained. These experiments were all conducted with the gas pressure less than confining pressure in order to avoid rupturing the rubber membrane. The flow outlet is left open, which means the outlet pressure is equal to atmospheric pressure, connecting the flow outlet to the gas flow meter and then recording data when the gas flow velocity became stable.

During the test, various combinations of inlet pressure and the confining stress were applied to the specimens. Figure 4 shows the test plan. The test comprised a series of loading–unloading cycles with several stress stages. For each stress stage, the gas inlet pressure was maintained a specific pressure (0.3 MPa). In the test, the effective stress was taken into account. As the inlet pressure was increased, the total confining stress was also increased to maintain a constant effective stress. For calculating the corresponding total confining stress, the Biot theory was used and the Biot coefficient was assumed to be 1 [19]. The gas pressure in the fracture was assumed to be the average of the inlet and the outlet pressures. Four fracture conductivity tests at 0–10 MPa effective stress under the same cyclic loading and unloading conditions were performed. According to the principle of effective stress [20], the confining pressure equals the sum of the effective stress and the fluid pressure in the fracture. Thus:

$$\sigma = \sigma' + p \tag{1}$$

where σ' is the effective stress (MPa); σ stands for confining pressure (MPa); p is the gas pressure in the specimen (MPa).

For these experiments, the effective stress in the middle portion of specimen can be approximated by Eq. 2:

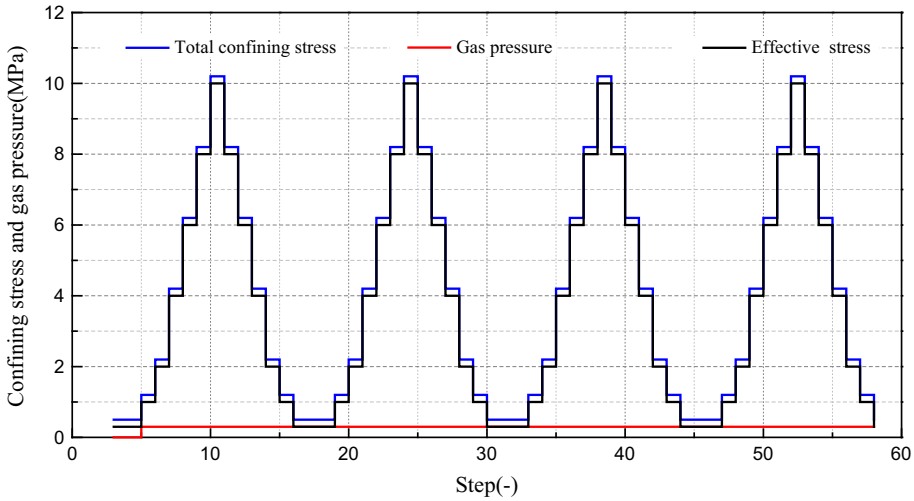

Fig. 4 Temporal development of pressure and stress in the triaxial loading tests

$$\sigma' = \sigma - \frac{1}{2}\left(p_{\text{in}} + p_{\text{out}}\right) \tag{2}$$

where p_{in} and p_{out} are the gas pressure at the inlet and the outlet, respectively (MPa). The value for p_{out} is the atmospheric pressure and that is, ideally, 0.1013 MPa.

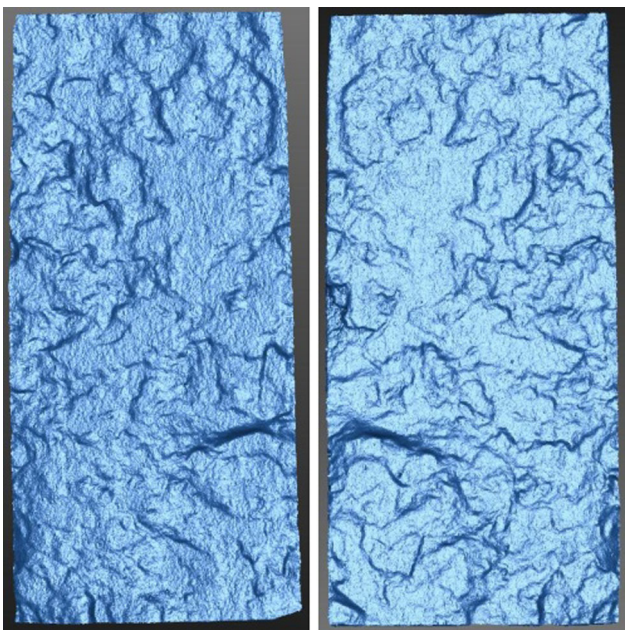

Fig. 5 Scanned images of the fracture surfaces for specimen S1

3 Results and Discussion

3.1 Fracture Surface Roughness

Figure 5 shows scanned images for both sides of specimen S1's fracture surface. The image shows that the fracture surface resulting from splitting the specimen along a bedding plane is not smooth. Table 1 lists the parameters for the fracture surfaces of the three specimens. The scanned surface areas of specimens S1, S2, and S3 are, respectively, 1.148, 1.128, and 1.069 times the nominal surface areas of those specimens (the nominal surface area is the area obtained by multiplying the measured length by the measured width of the specimen) [21]. The surface area ratios shown in Table 1 mean that the area added by asperities is the largest for specimen S1 and the S1 fracture surface is the roughest. The surface area ratios for specimens S2 and S3 are smaller and their fracture surfaces less rough.

3.2 Gas Flow

During the test, the flow rate at the outlet was measured. Because gas is compressible, the flow rate in the fracture is different from that at the outlet. In this analysis, the flow rate in the middle of the fracture was the flow rate considered. When the gas is under isothermal conditions, the flow rate

Table 1 Fracture surface area parameters for specimens S1, S2, and S3

Specimen	Length L (mm)	Width w (mm)	Nominal surface area (mm^2)	Measured surface area (mm^2)	Surface ratio (–)
S1	98.04	48.7	4774.55	5482.57	1.148
S2	98.1	49.2	4826.52	5443.75	1.128
S3	99.5	49.3	4905.35	5241.77	1.069

can be calculated from the following equation [22]:

$$Q_{\mathrm{m}} = Q_{\mathrm{out}} \frac{2p_{\mathrm{out}}}{p_{\mathrm{in}} + p_{\mathrm{out}}} \tag{3}$$

where Q_{m} and Q_{out} are the flow rate in the middle of the fracture and the outlet, respectively (m^3/s).

As shown in Fig. 6, fracture conductivity, as expressed by the gas flow rate, is affected by effective stress. At the initial stage of loading, the gas flow may decrease rapidly, but as the stress increases, the gas flow may decrease slowly. Because at the initial stage of loading, the area over which the fracture walls are in contact is relatively small and the tips of the asperities are under relatively great stress. This results in deformation of the fracture surface being relatively large. As deformation increases, the fracture contact area also increases and the specimen will be somewhat compacted. As a result, the gas flow will decrease more slowly. During unloading, nonrecoverable residual deformation on the fracture surface means that the gas flow is unable to return to its original value [23]. This is caused by the irreversible plastic deformation of the tips of the asperities on the rough fracture surface. The hysteresis in the gas flow is obvious. After one loading–unloading cycle, the hysteresis in flow between loading and unloading curves represents permanent damage to the fracture surface. The decrease in gas flow after the first cycle is the most significant. The gas flows for specimens S1, S2, and S3 decrease by 78.2, 65.5, and 56.3%, respectively. Then, as the number of loading–unloading cycles increases, the flow becomes stable. This means the nonrecoverable deformation on the fracture surfaces mainly occurs during the first loading. According to Table 1, at the same effective stress, the rougher the fracture surface, the lower the fracture conductivity.

3.3 Hydraulic Aperture

For theoretical analysis and modeling of flow in fractures, assuming that Darcy's law is valid and that the two fracture surfaces can be approximated by two smooth parallel planes, the flow rate per unit pressure gradient can be expressed as a linear function of the hydraulic aperture cubed, i.e., cubic law. In light of the results from conductivity experiment on gas flow through shale natural fractures, and the hydraulic aperture of middle part of specimen can be attained by cubic law (Eq. 4) [24]. For methane, the density is 0.648 $\mathrm{kg/m}^3$ and the dynamic viscosity is 11.1 μPa s under laboratory conditions [25].

$$w^3 = \frac{24\mu L p_{\mathrm{out}} Q}{b\left(p_{\mathrm{in}}^2 - p_{\mathrm{out}}^2\right)}. \tag{4}$$

where w is the hydraulic aperture (m); μ is the fluid dynamic viscosity (Pa s); L is the length of flow path (m); Q is the average flow rate (m^3/s); b is the width of the fracture surface (m).

The hysteresis in the hydraulic aperture is obvious (Fig. 7). The hysteresis of the hydraulic aperture is mainly caused by the nonrecoverable residual deformation on the fracture surface during loading and can be treated as damage to the

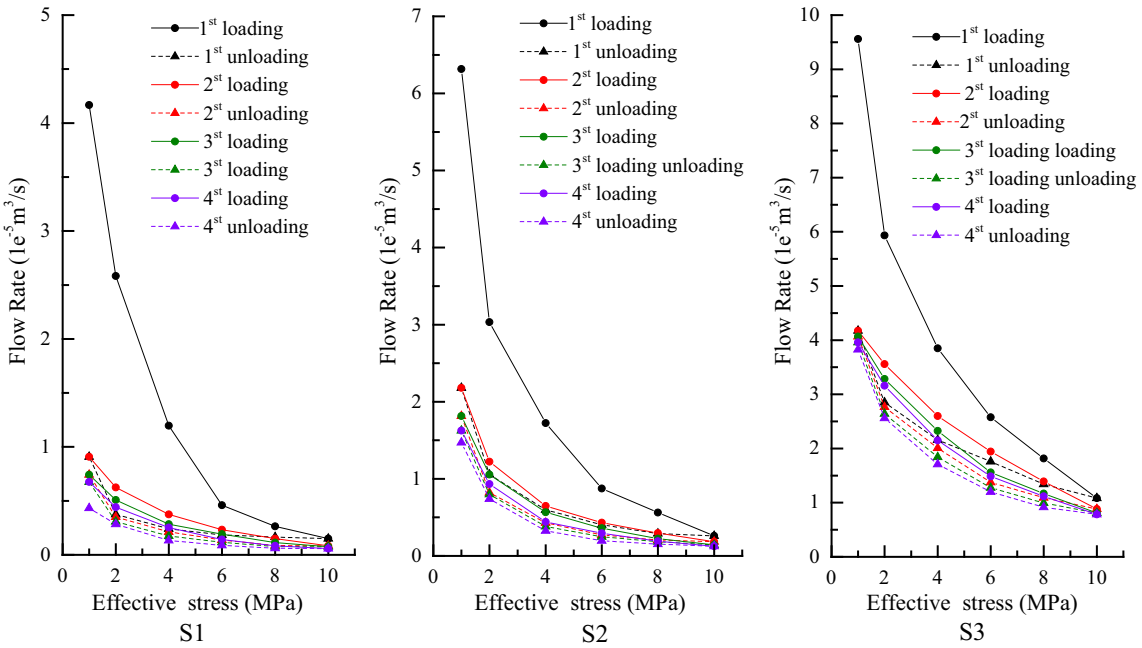

Fig. 6 Graphs of gas flow rate versus effective stress during four loading and unloading cycles for specimens S1, S2, and S3

hydraulic conductivity. Bandis [9] performed experiments on 65 groups of natural factures with different surface roughnesses and proposed a hyperbolic equation relating effective stress and fracture deformation. Under the influence of effective stress, the fracture mechanical aperture changes to cause a change in the fracture hydraulic aperture [26]. Therefore, the analysis presented here adopts the hyperbolic function to represent the relationship between fracture hydraulic aperture and effective stress. Thus:

$$w = a - \frac{b\sigma'}{c + \sigma'} \tag{5}$$

where w is the fracture hydraulic aperture of the specimen (m); σ' is the effective stress (MPa); a, b, and c are fitting parameters.

The normal rigidity of a shale fracture can be obtained through the derivation of Eq. 5, below.

$$\frac{\mathrm{d}w}{\mathrm{d}\sigma'} = -\frac{bc}{(c + \sigma')^2} = -\frac{1}{K} \tag{6}$$

where K is the normal rigidity of the fracture hydraulic aperture (MPa/m).

The first loading has the greatest influence on the fracture hydraulic aperture, and the hyperbolic function is adopted to fit the hydraulic aperture-effective stress curve during the first loading. The hyperbolic function contains three fitting parameters, a, b, and c, each of them with a different physical meaning. When the effective stress is zero, $w = a$, so "a" represents the initial hydraulic aperture before loading has started. When the effective stress tends to infinity, $w = a - b$, so "a–b" represents the residual hydraulic aperture of the fracture and "b" is the maximum variation of the hydraulic aperture. With increasing effective stress, the mechanical properties of the fracture will approach those of the rock matrix. Assuming that the residual conductivity of the fracture equals the permeability of the rock matrix and that the permeability is the average permeability ($0.028 \times 10^{-3}\,\mu\mathrm{m}^2$) of shale in the Silurian Longmaxi Formation in the East Sichuan Basin in China, the residual hydraulic aperture of the fracture under extremely great stress can be calculated. Using these assumptions, fitting the first loading hyperbolic curve to the formula gives "a–b" as a fixed value of 0.018 μm. In addition, when the effective stress is zero, the normal rigidity of the fracture $K = b/c$, where "c" is the fracture compressibility. When the confining pressure of effective stress is 10 MPa, the hydraulic apertures of S1, S2, and S3 are 10.19, 12.24, and 19.69 μm (Fig. 7). The endpoint of loading, 10 MPa, is the starting point for unloading. By considering the following several fittings of loading and unloading, at the first loading stage fitting, it should be ensure that the hyperbolic fitting curve passes the endpoint of 10 MPa.

As shown in Table 2, when the effective stress is zero (column "a"), the initial hydraulic apertures of S1, S2, and S3 are 41.35, 44.36, and 45.33 μm. After the first unloading, the fracture hydraulic apertures of S1, S2, and S3 cannot be completely recovered and the unrecoverable hydraulic apertures are, respectively, 12.28, 10.58, and 9.82 μm. These values are 28, 25, and 22% of the initial hydraulic apertures (the percent-

Table 2 Parameters used in Eq. 5 for fitting the hydraulic aperture during first loading

Specimens	a	b	c	Coefficient R
S1	41.34713	41.3288	3.80913	0.988
S2	44.3639	44.34557	3.26928	0.980
S3	45.33323	45.3149	7.68044	0.986

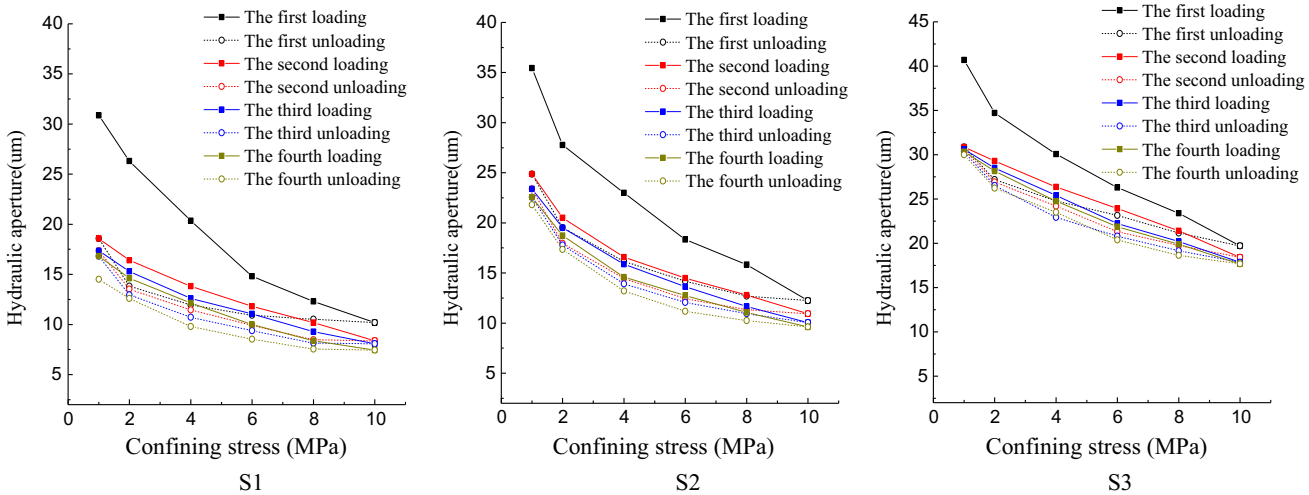

Fig. 7 Graphs showing how the hydraulic apertures of specimens S1, S2, and S3 change with effective stress during four cycles of loading and unloading

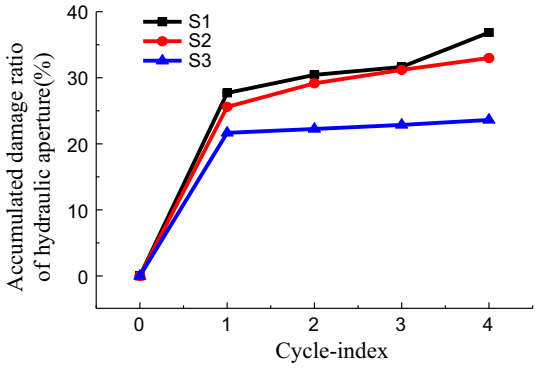

Fig. 8 Graph showing accumulated percentages of unrecoverable hydraulic aperture versus number of loading–unloading cycles

ages of unrecoverable hydraulic aperture). Figure 8 shows the accumulated percentages of unrecoverable hydraulic aperture versus the number of loading–unloading cycles. It can be seen that the rate at which the percentage of unrecoverable hydraulic aperture drops decreases, but the total accumulated unrecoverable aperture increases as the number of loading–unloading cycles increases. The first loading and unloading have the greatest effect on fracture conductivity. Compared to the first cycle, the percentage of aperture loss for the following three cycles amounts to less that 5% of the total aperture loss.

The fitting parameters a, b, and c have no physical significance when fitting the average values of all the unloading data and non-first cycle loading data to the hyperbolic curve. The normal fracture rigidity for different stress paths can be obtained from using the fitting parameters in Tables 2 and 3, and then, the rigidity can be applied in the following model to determine hydraulic aperture.

4 Theoretical Modeling and Verification

4.1 Hydraulic Aperture Modeling

Assume that the specimen is isotropic. At any given moment, the hydraulic aperture of a fracture can be represented by Eq. 7:

$$w_t = w_0 + \Delta w \tag{7}$$

where w_t is the fracture hydraulic aperture at the moment (m); w_0 is the fracture initial hydraulic aperture (m); Δw is the variation in the fracture hydraulic aperture (m).

During loading, the fracture hydraulic aperture decreases with the effective stress. During unloading, although the hydraulic aperture gradually recovers, the effective stress has already plastically deformed the fracture surface during loading, so the hydraulic aperture does not completely recover. Because the shale has undergone plastic deformation during loading, this study adopts the consolidation theory [27] from soil mechanics to establish a fracture hydraulic aperture model for a loaded condition.

The following formula is used to judge whether the fracture has reached a stressed condition for the first time:

$$F_c = \sigma'_{app} - \sigma'_{cap} \tag{8}$$

where σ'_{app} is the current effective stress (MPa) and σ'_{cap} is the maximum effective stress in the fracture loading history (MPa).

If $F_c > 0$, then the current effective stress has been loaded on the fracture for the first time; if $F_c \leq 0$, the current effective stress has appeared once in the fracture loading history. The variation of fracture hydraulic aperture equals the sum of plastic variation and elastic variation, so:

$$dw = dw_p + dw_e \tag{9}$$

where p represents plasticity and e represents elasticity. According to the fitting formula of the hyperbolic curve, the fracture normal rigidity can be obtained from the following equation. For the first loading:

$$\frac{dw_{t,F}}{d\sigma'} = -\frac{b_{L,F}c_{L,F}}{(c_{L,F} + \sigma')^2} = -\frac{1}{K_{t,F}} \tag{10}$$

For the non-first loading:

$$\frac{dw_t}{d\sigma'} = -\frac{b_L c_L}{(c_L + \sigma')^2} = -\frac{1}{K_{t,L}} \tag{11}$$

Table 3 Parameters used in Eq. 5 for fitting the hydraulic aperture for unloading and non-first loading

Specimens	Stress path	a	b	c	Coefficient R
S1	Non-first loading	19.89733	20.38681	7.49261	0.997
S1	Unloading	26.376	19.77003	1.05557	0.994
S2	Non-first loading	30.2185	24.14612	2.61397	0.997
S2	Loading	29.79429	22.85243	1.9295	0.999
S3	Non-first loading	32.45259	50.44112	25.14209	0.999
S3	Loading	34.46747	22.81272	4.34556	0.991

For the unloading:

$$\frac{\mathrm{d}w_\mathrm{e}}{\mathrm{d}\sigma'} = -\frac{b_\mathrm{U}c_\mathrm{U}}{(c_\mathrm{U}+\sigma')^2} = -\frac{1}{K_\mathrm{e}} \tag{12}$$

where F means the first loading, L means non-first loading, and U refers to unloading.

There are both elastic and plastic variations during loading but only elastic variations during unloading. Equations 10–12 can be used to obtain Eq. 13, the fracture plastic variation caused by stress change during loading.

$$\frac{\mathrm{d}w_\mathrm{p}}{\mathrm{d}\sigma'} = \frac{K_\mathrm{e}-K_t}{K_t K_\mathrm{e}} \tag{13}$$

The total variation in fracture hydraulic aperture for $F_\mathrm{c} > 0$ during loading is:

$$\begin{aligned}\mathrm{d}w &= \mathrm{d}w_\mathrm{e} + \mathrm{d}w_\mathrm{p,F} = -\frac{1}{K_{t,\mathrm{F}}}\mathrm{d}\sigma' \\ &= -\left(\frac{1}{K_\mathrm{e}} + \frac{K_\mathrm{e}-K_{t,\mathrm{F}}}{K_\mathrm{e}K_{t,\mathrm{F}}}\right)\mathrm{d}\sigma'\end{aligned} \tag{14}$$

For $F_\mathrm{c} \le 0$ during loading:

$$\begin{aligned}\mathrm{d}w &= \mathrm{d}w_\mathrm{e} + \mathrm{d}w_\mathrm{p,L} = -\frac{1}{K_{t,\mathrm{L}}}\mathrm{d}\sigma' \\ &= -\left(\frac{1}{K_\mathrm{e}} + \frac{K_\mathrm{e}-K_{t,\mathrm{L}}}{K_\mathrm{e}K_{t,\mathrm{L}}}\right)\mathrm{d}\sigma'\end{aligned} \tag{15}$$

For the unloading:

$$\mathrm{d}w = \mathrm{d}w_\mathrm{e} = -\frac{1}{K_\mathrm{e}}\mathrm{d}\sigma' \tag{16}$$

4.2 Verification

Based on the hydraulic aperture model described above, the model was written as subroutines by Visual Basic language to run inside the Microsoft Excel spreadsheet program (Microsoft Corp., Redmond, WA, USA). During stimulation, the stress path conditions are set to be identical to conditions during the experiments performed for this study. The Newton–Raphson method was adopted for each of the 1000 iterations in the 1 MPa loading and unloading steps to ensure that the calculations are as precise as possible.

Figure 9 shows the simulated fitting curves from the Excel calculations and the hydraulic aperture-effective stress points from Fig. 7 plotted together. It is clear that the simulated curves are basically identical to the curves on the actual hydraulic aperture plot. The plastic variation for the first loading–unloading cycle is the largest, and the subsequent loading–unloading cycles generate some plastic deformation, but the deformation is less than that generated by the

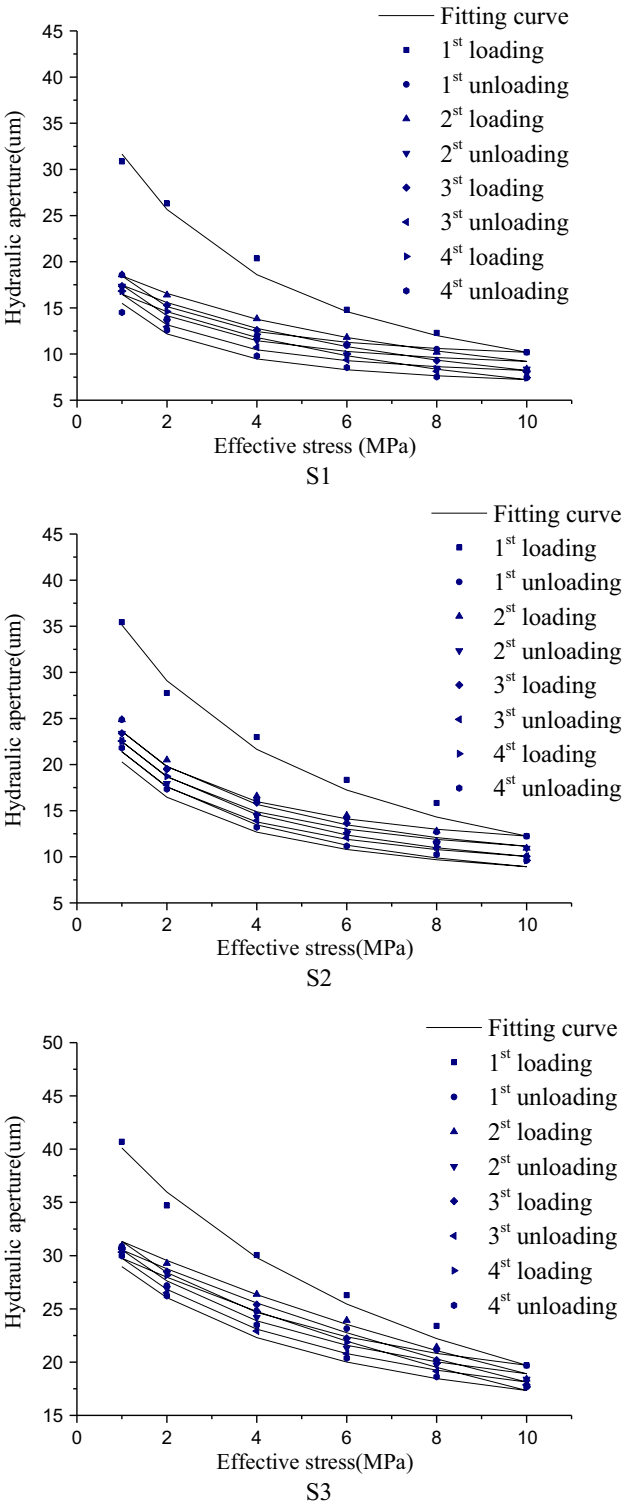

Fig. 9 Fitting curves calculated from the hydraulic aperture model plotted on the hydraulic aperture versus effective stress graphs showing the experiment results

first cycle. This is identical to the experimental results, as is the fact that there is no plastic deformation during unloading.

5 Conclusion

The stress loading history dependence on fracture conductivity in shale specimens was studied experimentally. Using a constant 0.3 MPa gas pressure, three shale specimens split by single fractures of different roughness were tested for gas flow during four loading–unloading cycles of 0–10 MPa. The result show a hysteresis in fracture conductivity during the loading and unloading, a hysteresis similar to that commonly observed during rock deformation tests. After the first cycle, the gas flow decreases significantly; the gas flow through the three specimens measured dropped by 78.2, 65.5, 56.3%. With an increase in the number of loading–unloading cycles, the gas flow gradually tends to stabilize. For the same experimental conditions, the gas flow through a fracture is smaller when the gas must flow through a fracture with a rougher fracture surface.

The magnitude of the hysteresis exhibited by the fracture hydraulic aperture depends on the plastic deformation of the fracture surface; the hysteresis increases as the extent of the plastic deformation increases. During the first loading cycle, the plastic deformation of the fracture surface is the greatest, whereas in the following cycles of loading and unloading, the hysteresis of the hydraulic aperture decreases significantly. The relationship between fracture hydraulic aperture and effective stress can be fitted by hyperbolic curves with a correlation coefficient of over 0.98. Based on the consolidation theory of soil mechanics, a hydraulic aperture fracture model is developed which takes the loading history into consideration. This model reflects the plastic and elastic deformation of the fractures during loading and unloading well and also reflects the influence of the loading history on the fracture hydraulic aperture. The mathematically simulated results from this model are nearly identical to the experimental data, and the model can provide valuable guidance for the prediction of fracture conductivity during actual gas production.

Acknowledgements The work is jointly supported by the National Key Basic Research Program of China (No. 2014CB239206), the National Natural Science Foundation of China (NSFC) (Nos. 51504043; 51404045), and the Program for Changjiang Scholars and Innovative Research Team in University of China (No. IRT13043).

References

1. Zhou, L.; Hou, Z.M.; et al.: Numerical investigation of a low-efficient hydraulic fracturing operation in a tight gas reservoir in the North German Basin. J. Pet. Sci. Eng. **120**, 119–129 (2014)
2. Tripathi, D.; Pournik, P.; et al.: Effect of acid on productivity of fractured shale reservoirs. SPE 1922960 (2014)
3. Zhou, T.; Zhang, S.C.; Feng, Y.; et al.: Experimental study of permeability characteristics for the cemented natural fracture of the shale gas formation. J. Nat. Gas Sci. Eng. **29**, 345–54 (2016)
4. Lomize, G.M.: Filtratsiya v treshchinovatykh porodakh. Gosenergoizdat, Moscow (1951)
5. Kranz, R.L.; Frankel, A.D.; Englder, T.; et al.: The permeability of whole and jointed Barre Granite. Int. J. Rock Mech. Min. Sci. **16**, 225–234 (1979)
6. Gale, J.E.: The effects of fracture type (induced versus natural) on the stress-fracture closure-fracture permeability relationships. In: Issues in Rock Mechanics 23rd Symposium on Rock Mechanics, pp. 290–298 (1982)
7. Tsang, Y.W.: The effect of tortuosity on fluid flow through a single fracture. Water Resour. Res. **20**, 1209–15 (1984)
8. Thompson, M.E.; Brown, S.R.: The effect of anisotropic surface roughness on flow and transport in fractures. J. Geophys. Res. **96**(B13), 21923–21932 (1991)
9. Bandis, S.; Lumsden, A.C.; Barton, N.: Fundamental of rock joint deformation. Int. J. Rock. Mech. Min. Sci. Geomech. Abstr. **20**, 249–268 (1983)
10. Barton, N.; Bandis, S.; Bakhtar, K.: Strength, deformation and conductivity coupling of rock fractures. Int. J. Rock Mech. Min. Sci. **22**, 121–40 (1985)
11. Barton, N.; Quadros, E.F.: Joint aperture and roughness in the prediction of flow and groutability of rock masses. Int. J. Rock Mech. Min. Sci. **34**, 3–4 (1997)
12. Zimmerman, R.W.; Chen, D.W.; Cook, N.G.W.: The effect of contact area on the permeability of fractures. J. Hydrol. **139**, 79–96 (1992)
13. Zimmerman, R.W.; Bodvarsson, G.S.: Hydraulic conductivity of rock fractures. Transp. Porous Media **23**, 1–30 (1996)
14. Guo, T.K.; Zhang, S.C.; Gao, J.; et al.: Experimental study of fracture permeability for stimulated reservoir volume (SRV) in shale formation. Transp. Porous Media **90**, 525–42 (2013)
15. Zhang, J.J.; Kamenov, A.; Zhu, D.; et al.: Measurement of realistic fracture conductivity in the Barnett shale. J. Unconv. Oil Gas Resour. **11**, 44–52 (2015)
16. Olsson, R.; Barton, N.: An improved model for hydromechanical coupling during shearing of rock joints. Int. J. Rock Mech. Min. Sci. **38**(3), 317–329 (2001)
17. Zhou, L.; Hou, M.Z.: A new numerical 3D-model for simulation of hydraulic fracturing in consideration of hydro-mechanical coupling effects. Int. J. Rock Mech. Min. Sci. **60**, 370–80 (2013)
18. Hickey, J.J.; Henk, B.: Lithofacies summary of the Mississippian Barnett Shale, Mitchell 2TP Sims well, Wise County, Texas. AAPG Bull. **33**(4), 437–443 (2007)
19. Biot, M.A.: General theory of three—dimensional consolidation. J. Appl. Phys. **12**(2), 155–164 (1941)
20. Terzaghi, K.; Peck, R.B.; Mesri, G.: Soil Mechanics in Engineering Practice, 3rd edn. Wiley, New York (1996)
21. Li, H.; Lu, Y.; Zhou, L.; et al.: Experimental and model studies on loading path-dependent and nonlinear gas flow behavior in shale fractures. Rock Mech. Rock Eng. **2**, 1–16 (2017)
22. Wyckoff, R.D.; Botset, H.G.; Muskat, M.; et al.: The measurement of the permeability of porous media for homogeneous fluids. Rev. Sci. Instrum. **4**, 394 (1993)
23. Roman, A.; Ahmadi, G.; Issen, K.A.; et al.: Permeability of fractured media under confining pressure: a simplified model. Open Pet. Eng. J. **5**(1), 36–41 (2012)
24. Witherspoon, J.S.Y.; Wang, K.I.; Gale, J.E.: Validity of cubic law for fluid-flow in a deformable rock fracture. Water Resour. Res. **16**, 1016–24 (1980)
25. Nist: Thermochemical Properties of Fluid Systems. http://webbook.nist.gov/chemistry/fluid/. Accessed 20 Oct (2016)

26. Goodman, R.E.; Taylor, R.L.; Brekke, T.A.: The mechanical properties of joints. In: Proceedings of the 3rd ISRM Congress, Held in Denver, USA 1A, pp. 127–140 (1974)

27. Wood, D.M.: Soil Behavior and Critical State Soil Mechanics. Cambridge University Press, Cambridge (1990)